

RESEARCH ARTICLE | SEPTEMBER 04 2008

Determination of complex refractive index of thin metal films from terahertz time-domain spectroscopy

Da-xiang Zhou; E. P. J. Parrott; Douglas J. Paul; J. Axel Zeidler



Journal of Applied Physics 104, 053110 (2008)

<https://doi.org/10.1063/1.2970161>



CrossMark



AIP Advances

Why Publish With Us?



25 DAYS
average time
to 1st decision



740+ DOWNLOADS
average per article



INCLUSIVE
scope

[Learn More](#)

 AIP
Publishing

Determination of complex refractive index of thin metal films from terahertz time-domain spectroscopy

Da-xiang Zhou,^{1,a)} E. P. J. Parrott,¹ Douglas J. Paul,² and J. Axel Zeitler³

¹*Cavendish Laboratory, University of Cambridge, J. J. Thomson Avenue, Cambridge CB3 0HE, United Kingdom*

²*Department of Electronics and Electrical Engineering, University of Glasgow, Glasgow G12 8LT, United Kingdom*

³*Department of Chemical Engineering, University of Cambridge, Cambridge CB2 3RA, United Kingdom*

(Received 11 February 2008; accepted 19 June 2008; published online 4 September 2008)

Thin metal films alone or incorporated in a multilayer stack structure with dielectric films are good candidates of terahertz absorbers necessary for achieving the maximum responsivity in microbolometer devices. However, the design and optimization of these absorber structures depend on the knowledge of the complex refractive index of metal films in the terahertz frequency range, which is not easy to measure or determine from experiment. This paper presents a novel method that allows fast and reliable extraction of the complex refractive index from terahertz time-domain spectroscopy. It starts with terahertz time-domain transmission measurements, followed by Fourier transforms to obtain the transmission spectrum in the frequency range of 0.1–3 THz, and finally an extraction process using the enhanced “on-the-downhill” algorithm. Some experimental examples are given, all of which show good agreement with theoretical calculations. This extraction method, combined with the scattering matrix model, can help design and optimize complicated absorber structures for terahertz microbolometers. © 2008 American Institute of Physics.

[DOI: 10.1063/1.2970161]

I. INTRODUCTION

Microbolometers are promising candidates for real-time terahertz imaging applications due to their low cost, room-temperature operation, and possibility of fabricating very large focal-plane arrays. For the maximum responsivity, each element in an array must be provided with a thermal absorber to convert incoming terahertz radiation into heat. Improving the optical performance of absorber structures for thermal detectors has been an old topic of research and two efficient solutions have been proposed. A single metal film can absorb at most 50% of the incident radiation.^{1,2} This absorption shows a quite constant value over the whole infrared (IR) band, and that explains the wide use of such films as efficient IR absorbers.³ Another promising solution is to form a quarter-wavelength ($\lambda/4$) structure^{4,5} by backing a thin metal film with a perfect reflector at $\lambda/4$ per optical distance, which can be adjusted using certain dielectric films. These $\lambda/4$ structures can increase the absorptivity from the 50% demonstrated in the single metal film absorbers to nearly 100%.

The design and optimization of the above absorber structures for terahertz microbolometers require a through knowledge of the complex refractive index of thin metal films in the terahertz spectral region. However, unfortunately most previous work that focused on the absorption theory of bolometers calculated the absorption using either the complex refractive index of thin metal films in the near- or mid-IR spectral region⁶ or the complex refractive index of bulk metal films.⁷ These values cannot be used to investigate the

absorption of bolometers in the terahertz spectral region as the complex refractive index of thin metal films is a sensitive function of the type and thickness of the metals and frequency. If the thickness of these thin metal films (nanometer range) is comparable to the metal grain size, bulk values of the complex refractive index or Drude model estimates from bulk measurements are not valid. Therefore in order to model the optical performance of thin-film metal absorber structures in the terahertz spectral region, we need to develop an efficient measurement technique and a data extraction method to obtain the complex refractive index of thin metal films.

We present in this paper a very fast and reliable extraction of the complex refractive index of nanometer-thick metal films from terahertz time-domain spectroscopy (TDS). Terahertz TDS is a powerful spectroscopic technique that generates and detects terahertz radiation in a synchronous and coherent manner.⁸ Using ultrashort electromagnetic pulses, terahertz TDS has given access to the complex refractive index of a wide range of materials, such as semiconductors,⁹ superconductors,¹⁰ dielectrics,¹¹ polymers,¹² pharmaceuticals,¹³ and liquids.¹⁴ We demonstrate here that terahertz TDS can even be used to characterize ultrathin metal films in the terahertz frequency range. The scattering matrix technique presented also allows the absorption of thin disordered films to be calculated where the Drude model is not valid.

II. THEORY

Consider a sample of thickness L with two flat and parallel surfaces [medium 2 in Fig. 1(b)], placed between two

^{a)}Electronic mail: dz221@cam.ac.uk.

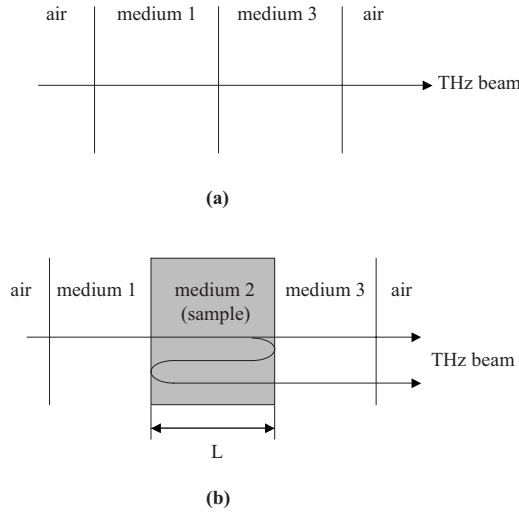


FIG. 1. Optical path of the terahertz beam in terahertz TDS for the (a) reference measurement and (b) sample measurement.

media, 1 and 3 (see Fig. 1). It assumes that all these three media are magnetically isotropic and have linear electromagnetic responses. The terahertz beam (plane wave with linear polarization) passes through the sample from medium 1 to medium 3 at normal incidence. With the above assumptions, the spectral component at angular frequency ω of the electric field of the terahertz wave transmitted from medium 1 to 3 without the sample [Fig. 1(a)] is given by

$$F_{\text{ref}}(\omega) = \eta(\omega) T_{13}(\omega) D_{\text{air}}(\omega, L) E(\omega), \quad (1)$$

where $\eta(\omega)$ is a term including all the transmission, reflection, and dephasing coefficients in media 1 and 3, $E(\omega)$ is the electric field of the terahertz wave emitted by the photoconductive emitter that serves as the terahertz source in terahertz TDS, $T_{ab}(\omega)$ is the transmission coefficient from medium a to medium b , and $D_a(\omega, d)$ is the dephasing coefficient in medium a over a distance d . The transmission and dephasing coefficients can be given by

$$T_{ab}(\omega) = \frac{2\tilde{n}_a}{\tilde{n}_a + \tilde{n}_b}, \quad (2)$$

$$D_a(\omega, d) = \exp\left[-j \frac{\tilde{n}_a \omega d}{c}\right], \quad (3)$$

where $\tilde{n}_a = n_a - j\kappa_a$ is the complex refractive index of medium a , which depends on the angular frequency ω , with n_a and κ_a being the real and imaginary parts of the refractive index, respectively.

When the sample is inserted between media 1 and 3 [Fig. 1(b)], the spectral component at angular frequency ω of the electric field of the terahertz wave transmitted through the sample is

$$F_{\text{sample}}(\omega) = \eta(\omega) \times T_{12}(\omega) \times D_2(\omega, L) \times T_{23}(\omega) \times E(\omega) \times \sum_{k=0}^{\infty} [R_{23}(\omega) \times D_2^2(\omega, L) \times R_{21}(\omega)]^k, \quad (4)$$

where $R_{ab}(\omega)$ is the reflection coefficient at the a - b interface, which can be given by

$$R_{ab}(\omega) = \frac{\tilde{n}_a - \tilde{n}_b}{\tilde{n}_a + \tilde{n}_b}. \quad (5)$$

The Fabry-Pérot effect in the sample (forward and backward reflections between the two flat and parallel surfaces) is represented by the term of summation.

The complex transmission coefficient of the sample, $T_{\text{sample}}(\omega)$, can be obtained by dividing the signal with the sample [$F_{\text{sample}}(\omega)$] by the signal without the sample [$F_{\text{ref}}(\omega)$].¹⁵

$$T_{\text{sample}}(\omega) = \frac{F_{\text{sample}}(\omega)}{F_{\text{ref}}(\omega)} = \frac{2\tilde{n}_2(\tilde{n}_1 + \tilde{n}_3)}{(\tilde{n}_2 + \tilde{n}_1)(\tilde{n}_2 + \tilde{n}_3)} \times \exp\left[-j(\tilde{n}_2 - \tilde{n}_{\text{air}}) \frac{\omega L}{c}\right] \text{FP}(\omega), \quad (6)$$

where $\text{FP}(\omega)$ represents the Fabry-Pérot term given by

$$\text{FP}(\omega) = \frac{1}{1 - \left(\frac{\tilde{n}_2 - \tilde{n}_1}{\tilde{n}_2 + \tilde{n}_1}\right) \left(\frac{\tilde{n}_2 - \tilde{n}_3}{\tilde{n}_2 + \tilde{n}_3}\right) \times \exp\left[-2j\tilde{n}_2 \frac{\omega L}{c}\right]}. \quad (7)$$

The complex transmission coefficient (including both amplitude and phase) of the sample can be measured experimentally by the terahertz TDS. Then the complex refractive index as a function of frequency can be self-consistently determined using an algorithm called “on-the-downhill” method, which solves the complex Eq. (6) with an accuracy set by the user.

III. ON-THE-DOWNHILL METHOD

One of the most efficient methods to solve a root finding problem is to use the Newton-Raphson algorithm.¹⁵ Unfortunately, this method could diverge easily if the function that we are looking for roots is oscillating. That is the case of the real and imaginary parts of $T_{\text{sample}}(\omega)$ as a function of n_2 and κ_2 . Therefore, the Newton-Raphson method is applicable only if one starts the calculation with values of n_2 and κ_2 very close to the final solution.

In contrast, the on-the-downhill method imposes no requirement on the starting values. The only restriction is that the function that we intend to find roots must be analytical. This method was originally proposed by Ward¹⁷ to solve any arbitrary analytical complex equation, $f(z) = f(x + jy) = 0$. Instead of searching for the zeros of $f(z)$, this algorithm defines a new function $W(x, y) = |R(x, y)| + |I(x, y)|$, where $R(x, y)$ and $I(x, y)$ are given by $f(z) = f(x + jy) = R(x, y) + jI(x, y)$, and searches for its zeros. This function is smooth and can be visualized as a surface always above the xy -plane. It is immediately seen that the zeros of $f(z)$ are also zeros of $W(x, y)$ and vice versa. The searching process involved in this method is based on the theorem that if $f(z)$ is analytical, then $W(x, y)$ has no minimum value such that $W \neq 0$. By working with the function $W(x, y)$ instead of $f(z)$, advantages may be taken of the above theorem.

The algorithm of the original on-the-downhill method can be described as follows. Let $P_1(x_1, y_1, W_1)$ be any point of the surface W . If $W_1=0$, $z_1=x_1+jy_1$ is a root of $f(z)$. Otherwise a neighboring point $P_2(x_2, y_2, W_2)$ exists for which $W_2 < W_1$. This point is said to be “downhill” from the first point, hence the name on-the-downhill. This process repeats until a final downhill $P_n(x_n, y_n, W_n)$ is reached for which $W_n < \Delta$ where Δ is a prescribed small positive number (for example, 1×10^{-6}), which determines the accuracy by which a root (x_0, y_0) is to be approximated. Theoretically, this method always converges toward a root provided that at least one root of $f(z)$ exists within a certain finite region of the xy -plane. However, in practice, it may fail to find a zero if any point in the downhill sequence P_1, P_2, \dots is a saddle point or trapped in a hollow or a valley.

The above dilemma can be solved by using an enhanced version of the on-the-downhill method.¹⁸ Let $z_k = x_k + jy_k$ be the k th iteration in the downhill sequence. Then three new test points $z_{k+1}^{(1)}$, $z_{k+1}^{(2)}$, and $z_{k+1}^{(3)}$ are calculated by

$$z_{k+1}^{(1)} = z_k + \delta e^{j\alpha} e^{j\theta}, \quad (8)$$

$$z_{k+1}^{(2)} = z_k + \delta e^{j\alpha}, \quad (9)$$

$$z_{k+1}^{(3)} = z_k + \delta e^{j\alpha} e^{-j\theta}, \quad (10)$$

where δ represents the step length between two consecutive iterations, α defines the angle between the center arm relative to the x -axis, and θ is the angle between the center arm and the two other arms. In this work an equilateral pattern is defined with $\alpha=0$ and $\theta=120^\circ$.

If a point $P_{k+1}(x_{k+1}, y_{k+1}, W_{k+1})$ calculated from the above three test points is found to be lower than the point $P_k(x_k, y_k, W_k)$, then the next downhill point P_{k+2} is searched in the direction determined by a line Q_k to Q_{k+1} , where Q_k and Q_{k+1} are the projections of P_k and P_{k+1} on the xy -plane. Thus the angle α is changed to a value given by

$$e^{j\alpha} = \frac{z_{k+1} - z_k}{|z_{k+1} - z_k|} = \frac{z_{k+1} - z_k}{\delta}. \quad (11)$$

Moreover, accordingly the arms are directed forward by setting $\theta=45^\circ$. This ensures that the test points are always searched in the neighboring region of the current downhill where the probability of finding the next downhill is greatest. In this way the speed of convergence can be greatly increased.

On the other hand, if no points are found lower to be than the current downhill P_k , special approaches have to be adopted to continue the downhill process. It is impossible to determine from the fact that $W_{k+1} > W_k$ whether the point P_k is trapped in a hollow or a valley (or a saddle point), and it has been shown that the approaches in these two situations are different.¹⁴ Our solution is to always at first assume that the current downhill point is in a hollow. Thus the step length δ is reduced by a prescribed factor (6.0 in this work), and if a downhill P_{k+1} is found, the above “forward search” procedure is continued from this point. If, however, a lower point is still not found, the above assumption that the current downhill is trapped in a hollow is abandoned, and instead we

assume that this downhill is in a valley (or a saddle point). Accordingly, the original step length is restored to avoid slow convergence, and the pattern for searching the three test points is rotated by setting α a new value (for example, 25° in this work) but keeping θ equal to 120° to maintain the equilateral pattern. If a lower point is found, the forward search procedure is continued as described above; if not, it is again assumed that this downhill is in a hollow, which is so narrow that the first reduction in step length is not sufficient. Therefore, a further reduction is performed and, if this still does not find a lower point, the pattern is rotated to a new angle (for example, multiples of 25°) to introduce extra arms. In this way, the search process is continued by changing between reductions in the step length and rotation of the pattern. It avoids unnecessary reductions in δ in a valley unless this valley is extremely narrow and therefore increases the speed of convergence.

IV. EXPERIMENT

The thin metal films were evaporated onto 600 μm thick high-resistivity bulk silicon substrates. These substrates provide low absorption with relatively flat monotonic frequency responses between the 0.1 and 3 THz frequencies of interest. For each evaporation session, the metal films were evaporated simultaneously on a bare silicon substrate and a photoresist-covered sample, which was prepatterned by standard optical lithography process. The thickness of the metal films was monitored during evaporation with a calibrated quartz crystal monitor. The actual thickness was measured on those prepatterned samples by a Dektak surface profiler. In this work, a number of metal samples, including Ti, NiCr, and Au thin films of different thicknesses, were fabricated and characterized. These metals were chosen for characterization due to their promising use as the terahertz absorbers and the ease of evaporation in our clean room.

The refractive index of the silicon substrate was measured by terahertz TDS prior to the metal film evaporation, which is almost constant ($n=3.42$) over the whole frequency range of measurement (0.1–3 THz). The terahertz TDS setup used in this work is a standard transmission mode of TDS.¹⁹ A Ti:sapphire laser provides visible/near-IR pulses of 12 fs duration at a center wavelength of 790 nm with a repetition rate of 76 MHz. The output is split into two parts: a 300 mW pump beam is focused onto the surface of a biased GaAs photoconductive emitter for terahertz generation and a 25 mW beam acts as the probe beam for electro-optic detection²⁰ using a 0.5 mm thick ZnTe crystal. The variable delay stage, which provides the time delay between the terahertz pulse and the probe pulse, is scanned over a distance of 7.5 mm, providing a spectral resolution of 0.015 THz. A signal-to-noise ratio of 10^5 is achieved by using a lock-in detection scheme. Data acquisition and processing are controlled by a computer program. For each sample, we made 20 measurements over which an average was taken to improve the accuracy of the measurements.

The extraction process starts with two terahertz time-domain transmission measurements, a reference one with the bare silicon substrate and a sample one with the substrate

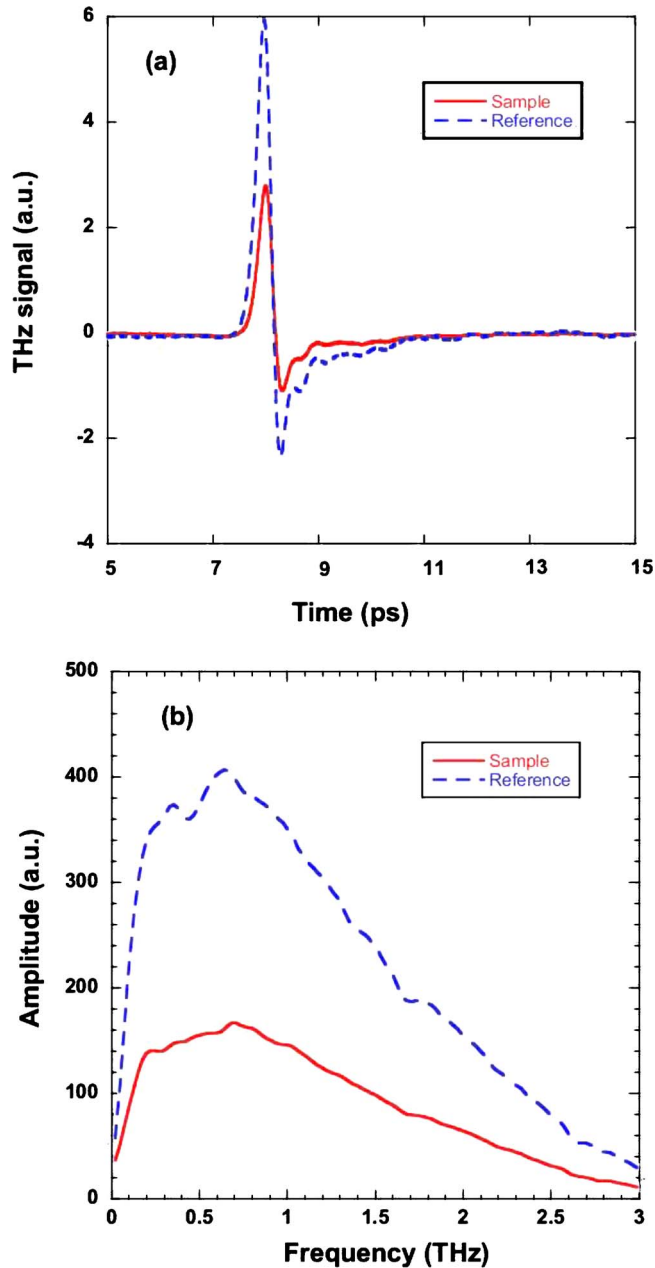


FIG. 2. (Color online) (a) Temporal terahertz waveform and (b) its corresponding Fourier-transform amplitude spectrum of the reference (bare Si substrate) and the sample (substrate covered by 21 nm Ti film).

covered by the thin metal film. This is followed by taking the ratio of the Fourier transforms of both time-domain signals to eliminate the substrate contribution and lead directly to the terahertz transmission spectrum of the metal film. The final step is concerned with the extraction of the complex refractive index using the on-the-downhill method, which is implemented in MATLAB in this work.

V. RESULTS AND DISCUSSION

Typical temporal waveforms and the corresponding Fourier-transform amplitude spectrum of the terahertz pulses for both the reference (bare silicon substrate) and the sample (substrate with 21 nm Ti) are shown in Fig. 2. The useful bandwidth is 0.03–3 THz and is mainly limited by the fre-

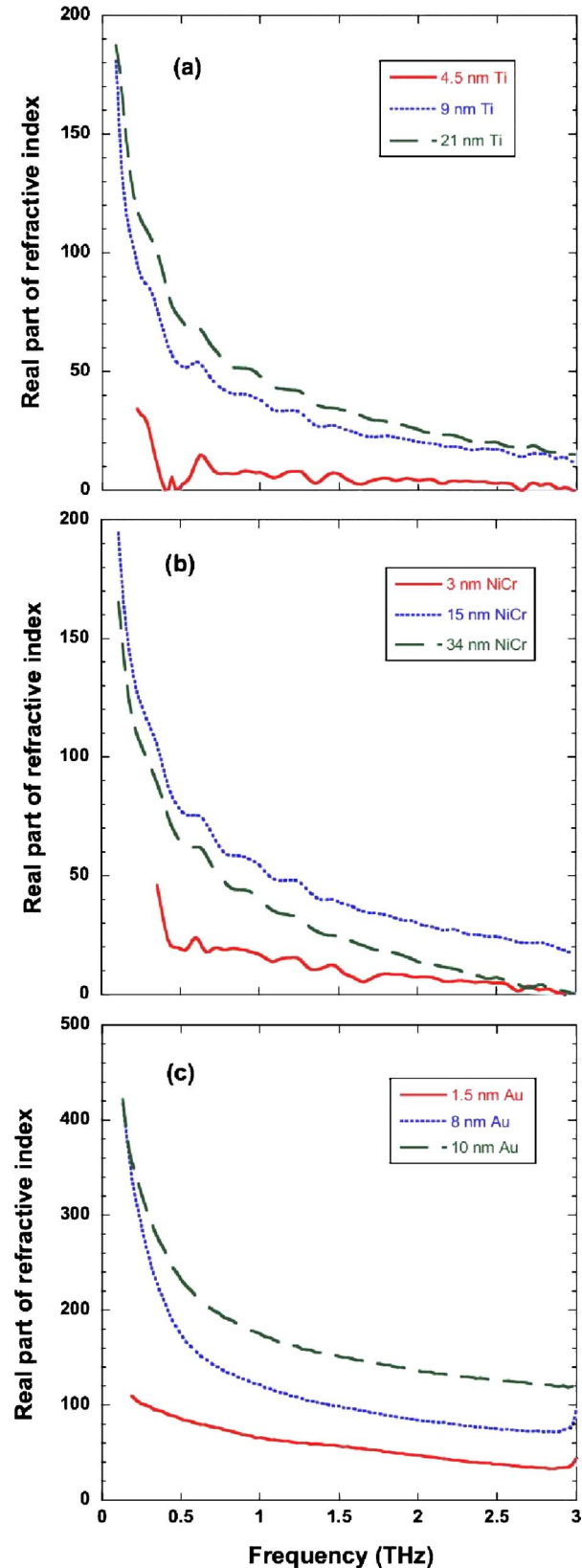


FIG. 3. (Color online) Real parts of the refractive index of thin metal films of different thicknesses: (a) Ti, (b) NiCr, and (c) Au.

quency response of the 0.5 mm thick ZnTe detector. The complex refractive index of the metal films versus frequency was determined from the experimental transmission spectrum using the on-the-downhill method. Figures 3 and 4

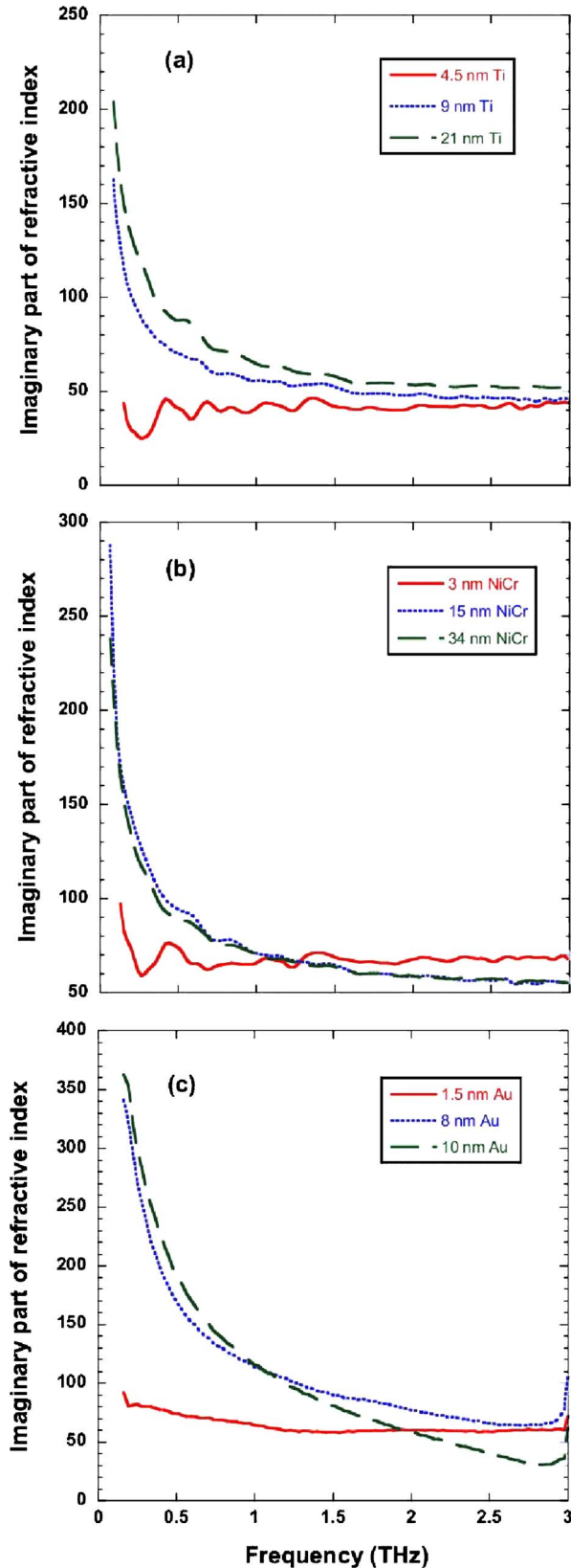


FIG. 4. (Color online) Imaginary parts of the refractive index of thin metal films of different thicknesses. (a) Ti, (b) NiCr, and (c) Au.

show, respectively, the real and imaginary parts of the refractive index of Ti, NiCr, and Au films for different thicknesses.

For small thicknesses (below 5 nm), both the real and imaginary parts of the refractive index are weak and constant

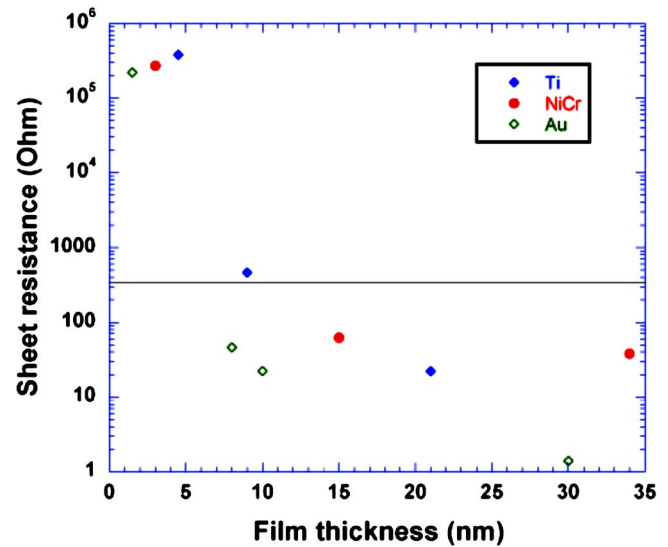


FIG. 5. (Color online) Measured sheet resistance of thin metal films of different thicknesses. The solid line indicates the free space impedance of 377 Ω .

over most of the measurement frequency range, which is characteristic of dielectric behavior. For thicker films, the real and imaginary parts of the refractive index vary more strongly with frequency, which is characteristic of metallic behavior. This change in behavior occurs when the film becomes continuous, which is expected at some critical thickness of order of the grain size of the metal. These ultrathin metal films consist of grains that are isolated when the thickness is far below this critical value. In this regime, only poor electrical conduction is allowed through hopping²¹ and therefore the film displays an electrically insulating, dielectric behavior. On the other hand, when the thickness is much larger than the critical value, those grains are in good contact and lead to a metallic response. For thicknesses around the critical value, hopping or percolation conduction dominates and film behavior shows a transition between those above two regimes.²¹ These characteristics have been confirmed by the measurement of film sheet resistance against thickness using the classical four-probe van der Pauw technique. Figure 5 shows the sheet resistance as a function of film thickness for various metals. It can be seen clearly that a transition of several orders of magnitude in the value of sheet resistance occurs for each metal. At small thicknesses, the sheet resistance is of the order of $10^5 \Omega$, similar to an electrically insulating dielectric material, while at much larger thicknesses, the sheet resistance rapidly reduces to below 100 Ω and decreases with the film thickness, which is characteristic of metallic behavior.

The validity and accuracy of our extraction method can be checked by comparing the experimental transmission spectrum obtained from the terahertz TDS with the theoretical calculations based on the scattering matrix model,²² which takes the complex refractive index as an input. The scattering matrix model treats the amplitudes of the electric vectors in successive media in a matrix notation, which generally can be used to characterize the optical performance of any multilayer structures consisting of an arbitrary number

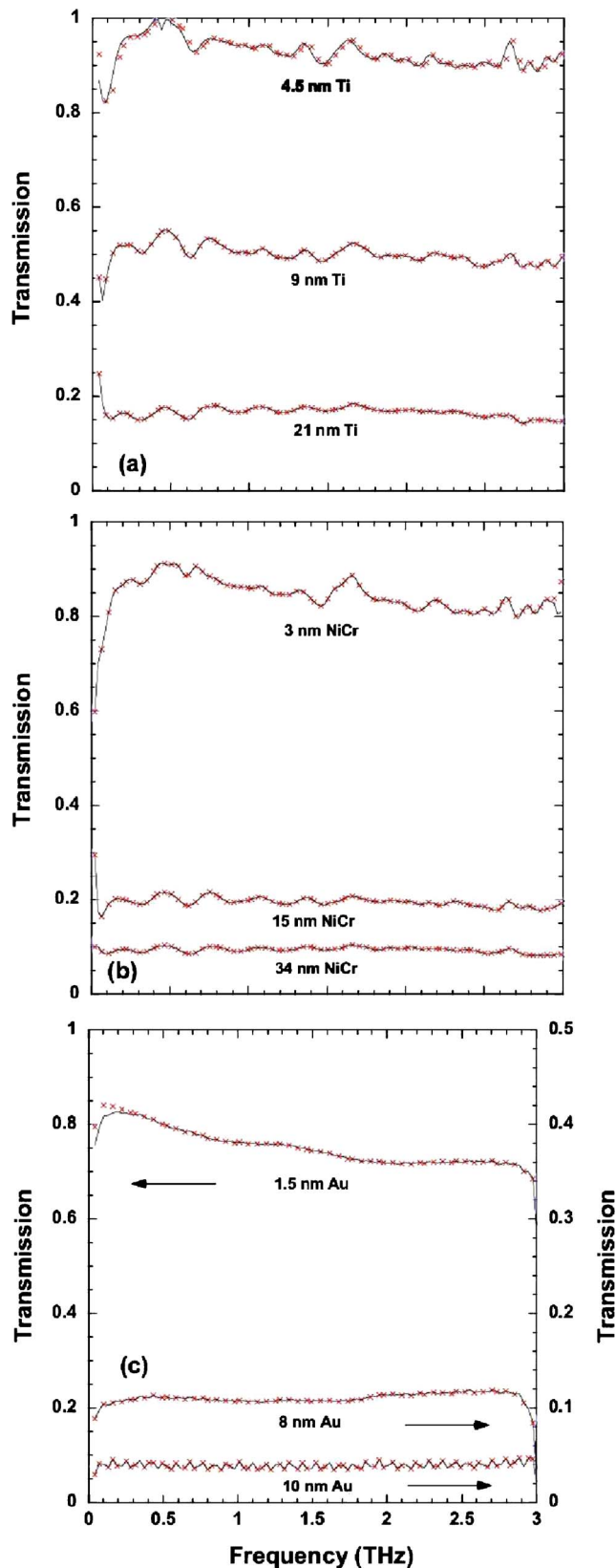


FIG. 6. (Color online) Transmission spectrum of (a) Ti, (b) NiCr, and (c) Au thin films of different thicknesses: experimental data (\times) and theoretical calculation (—).

of optical layers. Another attraction of this model is its ease of implementation by computer programs. In this work, a simple and efficient MATLAB program is implemented to calculate the transmission spectrum with the extracted complex

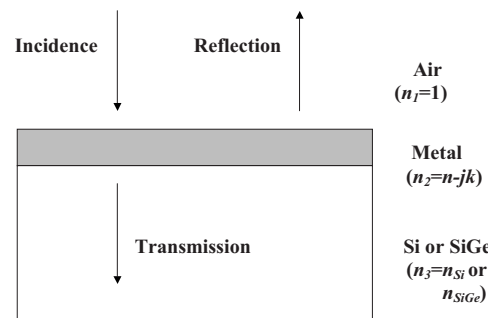


FIG. 7. Schematic of the three-layer optical system simulated by the scattering matrix model.

refractive index and the film thickness being input parameters. Figure 6 shows the comparison results for Ti, NiCr, and Au films of different thicknesses. The good agreement between the experimental and theoretical transmission spectra in all samples demonstrates that our extraction method based on terahertz TDS can provide an efficient and accurate approach to determine the complex refractive index of ultra-thin metal films in the terahertz spectral region.

Our extraction method, combined with the scattering matrix model described above, can be used to help design and optimize thin-film metal absorbers for terahertz microbolometers. By using the values of the complex refractive index and the thickness of the thin metal films, we can calculate the absorption, transmission, and reflection spectrum simultaneously based on the scattering matrix model. We assume that the thin metal films are on top of a transparent Si layer, which is the case for the microbolometer devices using thin metal films as the absorbers and high-resistivity Si materials as the sensing elements. Therefore, it has been modeled as a three-layer optical system (see Fig. 7), with air (with a refractive index of 1), metal film (with a complex refractive index extracted as above), and high-resistivity Si (with a refractive index of 3.42) being the corresponding constituent layers. It is also assumed that the absorption happens only in the thin metal film; thus, only the thickness of this layer is needed to do the calculation. On the other hand, the complex refractive index of all the three layers has to be provided as input parameters for the scattering matrix model.

Figure 8 shows the calculated absorption spectrum (transmission and reflection spectra are not shown) in the frequency range of 0.1–3 THz for Ti, NiCr, and Au samples of different thicknesses (corresponding to those samples of which the complex refractive index has been extracted from the terahertz TDS). Based on these calculations, we can determine the optimal thickness for each metal type at which the maximum possible absorption can be achieved. For example, we can conclude from Fig. 8 that the 8 nm Au film can lead to the highest and most stable absorption of 22% in the frequency range of 0–3 THz among all the metal samples we have measured. These information, together with some other physical parameters such as thermal mass, electrical conductivity, and lateral heat conductivity of the metal films, are essential for designing the optimal structures of real detectors.

It is worth mentioning that the optical properties of thin

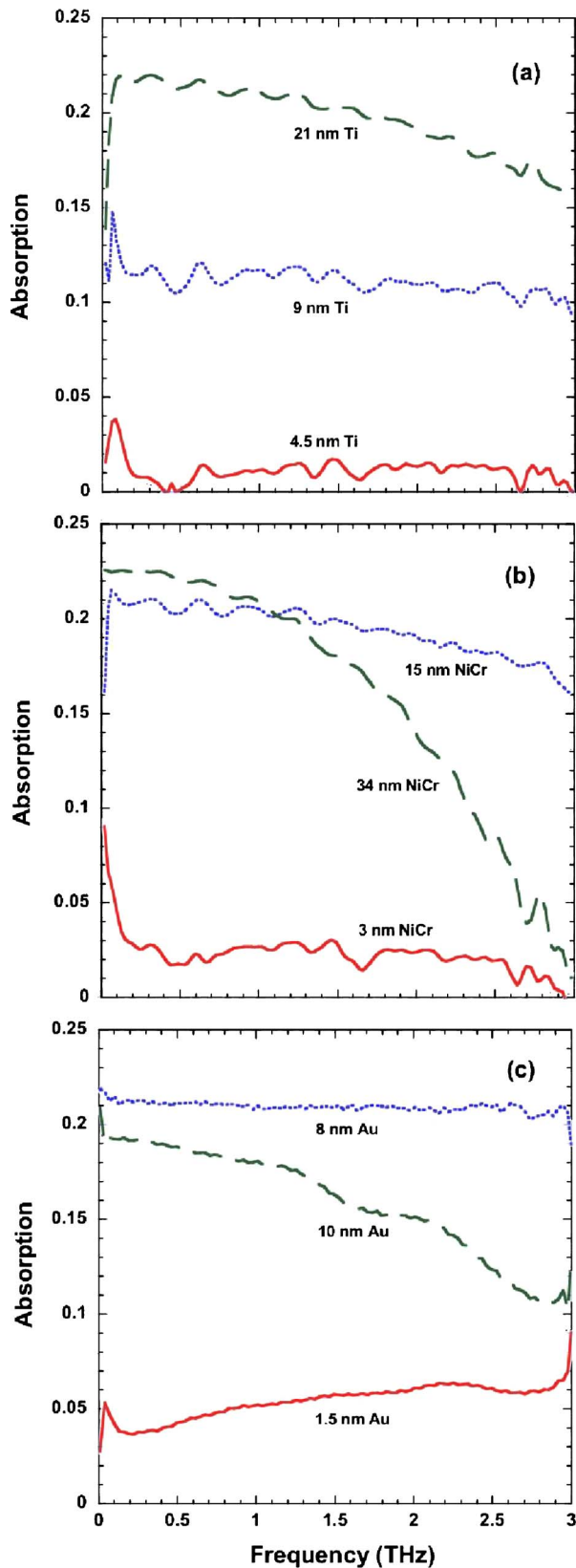


FIG. 8. (Color online) Calculated absorption of (a) Ti, (b) NiCr, and (c) Au thin films of different thicknesses from the scattering matrix model.

metal films can be discussed in a straightforward way in the frame of the Drude model of free electron charge carriers. For thin metal films on a dielectric substrate it is then straightforward to derive modified Fresnel reflection and transmission coefficient from an energy balance.²³

TABLE I. Calculated absorption of Ti, NiCr, and Au thin films of different thicknesses from the measured sheet resistance using the Drude model.

	Thickness (nm)	Sheet resistance (Ω)	Absorption
Ti	4.5	3.8×10^5	0.0001
	9	465	0.12
	21	22	0.15
NiCr	3	2.7×10^5	0.0001
	15	62	0.22
	34	38	0.19
Au	1.5	2.2×10^5	0.0003
	8	46	0.2
	10	22	0.15

$$r_{12} = \frac{n_1 \cos \theta_i - n_2 \cos \theta_t - f}{n_1 \cos \theta_i + n_2 \cos \theta_t + f}, \quad (12)$$

$$t_{12} = \frac{2n_1 \cos \theta_i}{n_1 \cos \theta_i + n_2 \cos \theta_t + f}, \quad (13)$$

where r_{12} and t_{12} are the reflection and transmission coefficients for an electromagnetic wave impinging on a boundary between two dielectric materials with complex refractive indices n_1 and n_2 , covered with a thin metal film with a sheet resistance R_s , θ_i and θ_t are the incident and transmitted angles, and f is the ratio of the vacuum impedance Z_0 (377 Ω) and the sheet resistance $f = Z_0/R_s$. By using this modified reflection and transmission coefficients, the reflection, transmission, and absorption of a thin metal film on a dielectric substrate can be calculated easily.

Table I shows the calculated absorption of Ti, NiCr, and Au films of different thicknesses using the Drude model and the measured sheet resistance. For all the thicknesses, the calculated absorption is nearly frequency independent. In contrast, the scattering matrix model gives frequency-independent absorption only for certain thicknesses (see Fig. 8). For other samples (21 nm Ti, 34 nm NiCr, and 10 nm Au) the absorption shows a strong dependence on the frequency. One possible explanation for these discrepancies is that the Drude model is only valid if the samples have clear bulk properties when the thicknesses are well above the threshold criteria for bulk metallic properties. Far below the transition regime, the films consist of separated grains with poor electrical conduction and display a dielectric behavior, thus leading to the failure of the Drude model. Far above the transition regime, the films can be regarded as completely homogeneous films composed of closely contacted grains and display a metallic behavior. Around the transition at certain critical thickness, hopping (percolation) conduction dominates and the Drude model fails again. These distinct regimes have been well demonstrated by our calculations.

A. Thin electrically insulating films

For the thinnest films used in this work (4.5 nm Ti, 3 nm NiCr, and 1.5 nm Au), the film thicknesses are well below the grain size and therefore not continuous. The electrical conductivity is dominated by hopping conduction and perco-

lation with large electrical sheet resistances, consistent with electrically insulating behavior.²¹ The Drude model is therefore not valid in this regime, but the scattering matrix model does allow calculation of the absorption of the films. The calculated values from the Drude model in Table I are significantly different from those obtained by the scattering matrix method. While some frequency dependence is demonstrated by the scattering matrix model, the amount is very small and relatively insignificant compared to errors in the measured input data.

B. Films close to metal-insulator transition

For films near the metal grain size (9 nm Ti, 15 nm NiCr, and 8 nm Au), the films are very close to a metal-insulator transition, and at room temperature there will be significant thermally activated hopping between grains providing electrical conduction.²¹ While at elevated temperatures, the high thermally activated hopping may provide high enough electrical conductivity that the Drude model may provide qualitative correct results, strictly speaking, only the scattering matrix model is valid in this regime. If samples are cooled to lower temperatures, then the Drude model will not be able to calculate the correct optical properties of the films as the electrical conductivity will reduce exponentially with temperature.²¹ Previously a scaling model has also been used to explain the optical properties of thin films comparable to the grain size,^{24,25} which provides similar results to the work in this paper. The key result in this scaling model²⁴ was that microscopic length scales, much smaller than the optical wavelength, determine the optical responses of materials at mid- and far-IR (terahertz) wavelengths. This work also demonstrated that both the Drude and effective-medium approach models should fail for films in this regime.^{24,25} The work in this paper on similar Au films demonstrates qualitatively similar properties for the optical properties of the films as demonstrated in Ref. 24. One issue discussed in Ref. 24 is the change in sheet resistance between the original fabrication and a couple of months later when Fourier-transform IR measurements were used to measure the optical properties. In such thin granular films, the optical properties of the films appear to be highly sensitive to aging, oxidation, and surface cleanliness issues.

C. Thick metallic films

For the thickest films (21 nm Ti, 34 nm NiCr, and 10 nm Au), the films started to behave as bulk metallic films, and so both the Drude and scattering matrix models should be valid above a particular film thickness close to these film thickness values. A frequency dependence is expected for bulk electrically conducting films as free carrier absorption should dominate the optical properties²⁶ while the films are still thin enough not to absorb all the radiation, and so the lower frequency absorption should be greater than the high frequency absorption as demonstrated in Fig. 8. This is most pronounced for the thickest film in the study, that of the 34 nm of NiCr, suggesting that the true bulk optical responses at these frequencies require films that are significantly thicker than the grain size in the films. A complete understanding of

this thickness would require a significantly larger number of film thicknesses to be studied, which is beyond the scope of the present paper.

The scattering matrix model combined with the measurement of sheet resistance against film thickness can help us better understand the behavior of metal film absorptions. Furthermore, it can help us determine the optimal thickness of various metal films at which the maximum absorption of 50% can be obtained. This information, along with considerations for low thermal mass and high reproducibility of thermal absorbers, can help us choose the most appropriate metal and film thicknesses for achieving the maximum responsivity in microbolometers.

VI. CONCLUSIONS

We have presented a novel method that allows reliable and real-time extraction of the complex refractive index of nanometer-thick metal films from terahertz TDS. This method involves terahertz time-domain transmission measurements, followed by Fourier transforms to obtain the complex transmission spectrum in the frequency domain, and finally an extraction process using the enhanced on-the-downhill algorithm. We have demonstrated its validity on three experimental examples (Ti, NiCr, and Au films), all of which have shown good agreement between experimental measurements and theoretical calculations. We have also demonstrated its use in designing and optimizing thin-film metal absorbers for terahertz microbolometers. This extraction method, combined with the scattering matrix model, can find a wide range of applications in the design and characterization of terahertz optical systems.

ACKNOWLEDGMENTS

The authors would like to acknowledge Cambridge Overseas Trust for financial support. The authors would also like to thank Dr. Mario Caironi from the Optoelectronics Group of the Cavendish Laboratory for assisting in the measurement of sheet resistance of our metal samples.

¹L. N. Hadley and D. M. Dennison, *J. Opt. Soc. Am.* **37**, 451 (1947).

²P. A. Silberg, *J. Opt. Soc. Am.* **47**, 575 (1957).

³A. Hadni and X. Gerbaux, *Infrared Phys.* **30**, 465 (1990).

⁴A. D. Parsons and D. J. Pedder, *J. Vac. Sci. Technol. A* **6**, 1688 (1988).

⁵S. Bauer, S. Bauer-Gogonea, and B. Ploss, *Appl. Phys. B: Photophys. Laser Chem.* **54**, 544 (1992).

⁶J. J. Monzon and L. L. Sanchez-Soto, *Appl. Opt.* **33**, 5137 (1994).

⁷B. Carli and D. Iorio-Fili, *J. Opt. Soc. Am.* **71**, 1020 (1981).

⁸C. A. Schmuttenmaer, *Chem. Rev. (Washington, D.C.)* **104**, 1759 (2004).

⁹M. Van Exter and D. Grischkowsky, *Appl. Phys. Lett.* **56**, 1694 (1990).

¹⁰J. F. Whitaker, F. Gao, and Y. Liu, *Proc. SPIE* **2145**, 168 (1994).

¹¹D. Grischkowsky, S. Keiding, M. Van Exter, and Ch. Fattinger, *J. Opt. Soc. Am. B* **7**, 2006 (1990).

¹²S. R. Keiding, *J. Phys. Chem. A* **101**, 5250 (1997).

¹³J. A. Zeitler, P. F. Taday, D. A. Newnham, M. Pepper, K. C. Gordon, and T. Rades, *J. Pharm. Pharmacol.* **59**, 209 (2007).

¹⁴J. Pedersen and S. Keiding, *IEEE J. Quantum Electron.* **28**, 2518 (1992).

¹⁵L. Duvallet, F. Garet, and J.-L. Coutaz, *IEEE J. Sel. Top. Quantum Electron.* **2**, 739 (1996).

¹⁶W. H. Press, B. P. Flannery, S. A. Teukolsky, and W. T. Vetterling, *Numerical Recipes in C++* (Cambridge University Press, Cambridge, England, 2002).

¹⁷J. A. Ward, *J. ACM* **4**, 148 (1957).

¹⁸M. Onoe, *Commun. ACM*, **5**, 398 (1962).

- ¹⁹Y. C. Shen, P. C. Upadhyaya, A. G. Davies, and E. H. Linfield, *J. Biol. Phys.* **29**, 135 (2003).
- ²⁰Q. Wu and X.-C. Zhang, *Appl. Phys. Lett.* **70**, 1784 (1997).
- ²¹N. F. Mott, *Metal Insulator Transitions* (Taylor & Francis, London, 1990).
- ²²O. S. Heavens, *Rep. Prog. Phys.* **23**, 1 (1960).
- ²³S. Bauer, *Am. J. Phys.* **60**, 257 (1992).
- ²⁴Y. Yagil, P. Gadenne, C. Julien, and G. Deutscher, *Phys. Rev. B* **46**, 2503 (1992).
- ²⁵Y. Yagil, M. Yosefin, D. J. Bergman, G. Deutscher, and P. Gadenne, *Phys. Rev. B* **43**, 11342 (1991).
- ²⁶K. Seeger, *Semiconductor Physics: An Introduction*, 9th ed. (Springer-Verlag, Heidelberg, 2004).